Geophysical Research Letters®

Key Points:

- The spatial distributions of cold and hot patches respond well to the convection pattern for different interplanetary magnetic field orientations
- The hot patches are more frequent at lower magnetic latitudes than cold patches, and located closer to the auroral oval
- Enhanced anti-sunward flow promotes cold patch occurrence under $Bz < 0$, and soft-electron precipitation promotes hot patch occurrence

The Dependence of Cold and Hot Patches on Local Plasma Transport and Particle Precipitation in Northern Hemisphere Winter

Duan Zhang[1] [iD]**, Qing-He Zhang[1]** [iD]**, Y.-Z. Ma[1]** [iD]**, Kjellmar Oksavik[2,3]** [iD]**, L. R. Lyons[4]** [iD]**, Zan-Yang Xing[1]** [iD]**, Marc Hairston[5]** [iD]**, Z.-X. Deng[6], and J.-J. Liu[7]** [iD]

[1]Shandong Provincial Key Laboratory of Optical Astronomy and Solar-Terrestrial Environment, Institute of Space Sciences, Shandong University, Weihai, China, [2]Department of Physics and Technology, Birkeland Centre for Space Sciences, University of Bergen, Bergen, Norway, [3]Arctic Geophysics, University Centre in Svalbard, Longyearbyen, Norway, [4]Department of Atmospheric and Oceanic Sciences, University of California, Los Angeles, CA, USA, [5]William B. Hanson Center for Space Sciences, University of Texas at Dallas, Richardson, TX, USA, [6]National Key Laboratory of Electromagnetic Environment, China Research Institute of Radiowave Propagation, Qingdao, China, [7]Polar Research Institute of China, Shanghai, China

Abstract By using a database of 4,634 cold patches (high density and low electron temperature) and 4,700 hot patches (high density and high electron temperature) from Defense Meteorological Satellite Program F16 in 2005–2018 winter months (October–March), we present a statistical survey of the distributions of polar cap patches for different interplanetary magnetic field (IMF) orientations and ionospheric convection geometries. We investigate the dependence of cold and hot patches on local plasma transport and soft-electron precipitation. Our results indicate that: in winter, (a) more cold and hot patches occur in the stronger anti-sunward flow organized by different IMF orientations. (b) cold patches are frequent near the central polar cap, while hot patches are closer to the auroral oval. (c) enhanced anti-sunward flow ($E \times B$ drift) mainly contributes to cold patch occurrence under $Bz < 0$, and soft-electron precipitation contributes to hot patch occurrence both under southward and northward IMF.

Plain Language Summary Polar cap patches are common phenomena in the polar ionosphere and consist of high-density plasma. We use 4,634 cold patches and 4,700 hot patches observed by the Defense Meteorological Satellite Program to investigate the distributions of polar cap patches for different interplanetary magnetic field (IMF) orientations and ionospheric convection geometries. We find that more cold and hot patches are distributed in areas of stronger anti-sunward flow in winter. The hot patches are more frequent at lower magnetic latitudes, and located closer to the auroral oval than cold patches. Furthermore, in winter months, higher anti-sunward flow velocity mainly contributes to a higher occurrence of cold patches under southward IMF, and stronger soft-electron precipitation mainly contributes to a higher occurrence of hot patches both under southward and northward IMF.

1. Introduction

Polar cap patches are common phenomena in the polar ionospheric F region. They are plasma structures whose densities are at least twice that of the surrounding regions, with a typical size ranging from hundreds to thousands of kilometers (e.g., Carlson, 2012; Coley & Heelis, 1995; Crowley, 1996; Weber et al., 1984; Zhang, Zhang, Hu et al., 2013). Polar cap patches are usually formed near the dynamic cusp due to magnetic reconnection (e.g., Lockwood & Carlson, 1992; Zhang, Zhang, Lockwood et al., 2013) and move along the ionospheric convection streamlines from the dayside across the polar cap, and then into the nightside auroral oval (e.g., Dungey, 1961; Nishimura et al., 2014; Oksavik et al., 2010; Zhang, Xing et al., 2020; Zhang, Zhang, Hu et al., 2013, Zhang et al., 2015, 2016). As polar cap patches move, strong electron density gradients can occur along at their edges, which may cause strong scintillations of trans-ionospheric signals in the polar cap (Zhang et al., 2017). Understanding the key features of polar cap patches is thus of key importance for the space weather community.

Previous studies have found that polar cap patches can be divided into two groups based on their ion/electron temperature (Ti/Te) (Ma, Zhang, Xing, Heelis et al., 2018): (a) cold patches (Ti/Te > 0.8) that are transported from dayside sunlit areas in the midlatitude ionosphere; and (b) hot patches (Ti/Te < 0.8) that are stimulated by

particle precipitation (e.g., Goodwin et al., 2015; Zhang et al., 2010, 2017). Both cold and hot patches are generated by dynamic solar wind-magnetosphere-ionosphere coupling processes (e.g., Carlson et al., 2004; Oksavik et al., 2010; Zhang, Zhang, Lockwood et al., 2013). Their occurrence also depends on the IMF orientation (e.g., Jin et al., 2019; McEwen & Harris, 1996). Moreover, the cold and hot patches' statistical dependence on solar and geomagnetic activity has been investigated (Zhang et al., 2021).

However, the specific influence of IMF orientations and ionospheric convection geometries on the key features of cold and hot patches has not been systematically studied. Still, it is important for understanding and predicting space weather effects in the polar ionosphere. In this study, we have surveyed a database of 4,634 cold patches and 4,700 hot patches from the Defense Meteorological Satellite Program (DMSP) F16 for the years 2005–2018 winter months (October–March) (Zhang et al., 2021) to identify the distributions of polar cap patches for different IMF orientations and ionospheric convection geometries. We discuss how cold and hot patches depend on local plasma transport and soft-electron precipitation. Note that there are not enough patches observed in other months, so we only consider the patches in winter months.

2. Data Sources and Methodology

The DMSP satellites are three-axis stabilized spacecraft in ∼835–860 km altitude and with orbital periods of ∼101 min. The Precipitating Electron and Ion Spectrometer (SSJ/4) (http://cedar.openmadrigal.org/list/) (e.g., Hardy et al., 1984) onboard the DMSP satellites offers the differential energy fluxes of precipitating electrons and ions from 32 eV to 30 keV. The Special Sensor for Ions, Electrons and Scintillation (https://satdat.ngdc.noaa.gov/dmsp/data/) (e.g., Greenspan et al., 1986) offers ion and electron densities (Ni and Ne), and ion and electron temperatures (Ti and Te).

The IMF data, was obtained from the OMNI website (http://omniweb.gsfc.nasa.gov), which gives the IMF propagated to the magnetopause. In this study, we apply 7 min delay (Hu et al., 2017) to all OMNI data to account for the solar wind response time from the subsolar magnetopause to the dayside ionosphere.

We also use the high-latitude convection model developed by Pettigrew et al. (2010) to relate the spatial distributions of polar cap patches to ionospheric convection. It is an empirical statistical model using line-of-sight (LOS) horizontal plasma drift from the Super Dual Auroral Radar Network (SuperDARN). In the model the high-latitude convection electric field is parameterized in terms of the IMF orientation/magnitude and dipole tilt angle. The dipole tilt angle is calculated using the International Geomagnetic Reference Field model (Mandea & Macmillan, 2000). Negative tilt (tilt < −10°) is winter in the northern hemisphere (NH), positive tilt (tilt > 10°) is summer in the NH, and neutral tilt (−10° < tilt < 10°) is for equinox. In this study, we used the mode for magnitude of the transverse component of the IMF ($B_T = \sqrt{By^2 + Bz^2}$) between 3 and 5 nT, and negative tilt (since polar cap patches primarily occur in winter months (e.g., Spicher et al., 2017; Zhang et al., 2021)).

The auroral oval model used in this paper is developed by Yang et al. (2016) based on IMF, solar wind velocity (V_p) and density (N_p), and geomagnetic parameters (AE). This model gives the poleward and equatorward boundaries of ultraviolet auroral oval. The Mean Absolute Deviation for the poleward and equatorward boundaries of the auroral oval is around 1.55 and 1.66° magnetic latitude (MLAT), which is superior to other similar models. For better consistency with the convection model used in the current paper, we set the input parameter as $B_T = 4$ nT, $Vp = 350$ km/s, $N_p = 4$ cm^{-3}, and AE = 50 nT.

The paper by Zhang et al. (2021) describes the automatic identification and classification method of polar cap patches in detail, which involves three steps: (a) The polar cap boundaries are identified based on the high-energy particle precipitation cutoff and the convection reversal. (b) The regions where the densities are two times higher than the averaged polar cap density are classified as patches (Ma, Zhang, Xing, Jayachandran et al., 2018). (c) These patches are divided into cold and hot patches using the Ti/Te ratio of Ma, Zhang, Xing, Heelis et al., 2018: cold patches, Ti/Te > 0.8; hot patches, Ti/Te < 0.8. Two typical patches observed by the DMSP F16 satellite as it crossed the polar region are shown in Figure S1 (modified from Zhang et al., 2017; Zhang et al., 2021) in Figure S1. The cold patch occurred in the central polar cap, and the hot patch occurred near the dawnside auroral oval. In addition, the hot patch was associated with strong flow shears and particle precipitation, which were different from the cold patch.
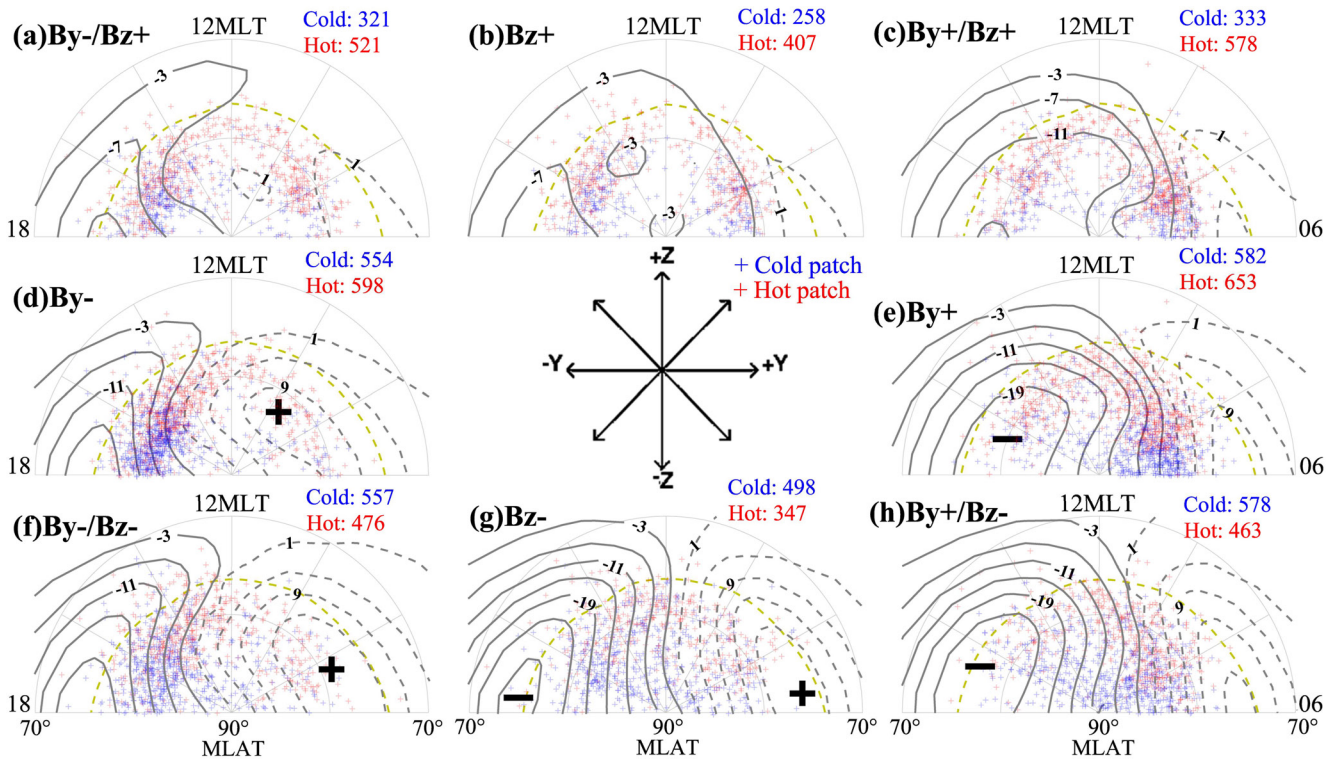
Figure 1. The spatial MLAT-MLT distributions of the dayside cold (blue) and hot (red) patches superimposed on the statistical ionospheric convection patterns (electrostatic potentials in kV, gray lines) for eight 45°-wide clock angles centered about θ = (a) −45°, (b) 0°, and (c) 45°, and so on. The yellow lines highlight the statistical poleward boundary of the auroral oval. The numbers of cold and hot patches are marked in the upper right corner of each panel.

3. Statistical Results

We consider the 4,634 cold patches and 4,700 hot patches in the DMSP F16 data in 2005–2018 winter months of Zhang et al. (2021). Figure 1 shows the spatial MLAT-magnetic local time (MLT) distributions of the dayside cold (blue) and hot (red) patches superimposed on the statistical ionospheric convection patterns (electrostatic potentials, gray lines) for eight 45°-wide clock angle (θ = atan (By/Bz)) intervals centered about θ = (a) −45°, (b) 0°, and (c) 45°, and so on. The IMF By and Bz are calculated by the median during the period each patch was observed. The yellow dashed lines highlight the statistical poleward boundary of the ultraviolet auroral oval. Only a small fraction of the identified polar cap patches (∼1% cold patches, ∼3% hot patches) lie equatorward of the statistical auroral boundary, reflecting limitations of the boundary model and that some patches may occur near the auroral oval, such as induced by poleward moving auroral forms (PMAFs) (e.g., Hosokawa et al., 2016), which are very close to the auroral oval. The numbers of cold and hot patches are marked in the upper right corner of each panel, and reveal that cold patches preferentially appear under southward IMF (Crowley, 1996). Figure 1 indicates that the spatial distributions of cold and hot patches are well organized by the IMF convection patterns, with highest occurrence around strong anti-sunward flow within the polar cap except for northward IMF. However, a portion of the patches seems to appear outside of the area of anti-sunward flow, as is expected since the statistical model is unable to capture transient events. Moreover, both cold and hot patches show an apparent IMF By-related prenoon-postnoon asymmetry, and the hot patches tend to be closer to the poleward boundary of the auroral oval than the cold patches.

Figure 2 shows the MLAT versus clock angle distributions of (a1–a4) patch occurrence, (b1–b4) O^+ density, (c1–c4) electron temperature (Te), (d1–d4) soft-electron (<1 keV) energy flux, and (e1–e4) the cross-track velocity ($V_{\text{cross-track}}$). These parameters are the medians of the values throughout each patch. The two columns on the left correspond to cold patches, and the two columns on the right correspond to hot patches. To separate patches between the dawn and dusk side, we divide the events in two groups: 6–12 MLT and 12–18 MLT. The data points are binned with 1° MLAT and 10° clock angle. The black/magenta lines in panels a1–a4 identify the MLAT with the highest patch occurrence versus clock angle (the magenta dashed lines in panels a1–a2 are overlaid from the

Figure 2. Magnetic latitude (MLAT) versus clock angle distributions of (a1–a4) patch occurrence, (b1–b4) O$^+$ density, (c1–c4) electron temperature (Te), (d1–d4) soft-electron (<1 keV) energy flux, and (e1–e4) the cross-track velocity ($V_{cross-track}$). The two columns on the left correspond to cold patches, and the two columns on the right correspond to hot patches. The distributions are binned over 1° MLAT and 10° clock angle. The black/magenta lines in panels a1–a4 identify the MLAT with the highest patch occurrence versus clock angle (the mage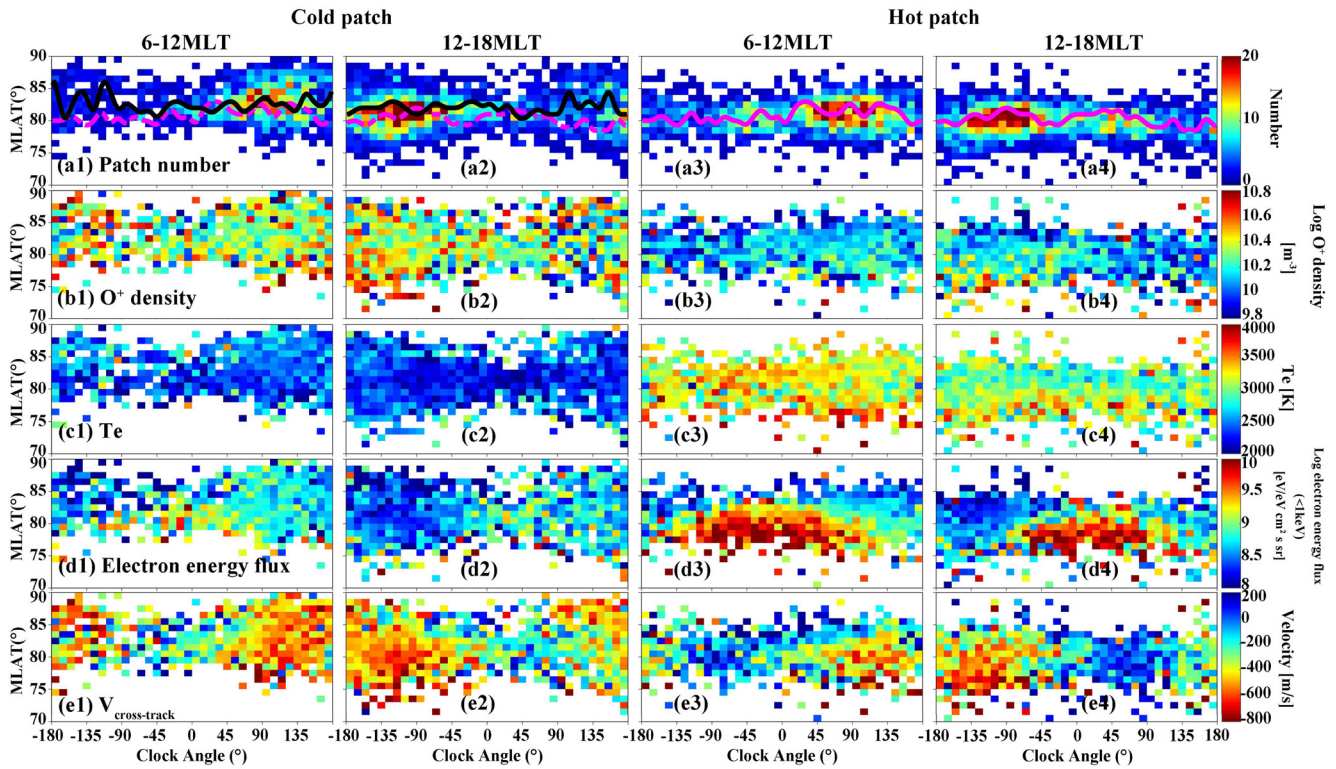nta dashed lines in panels a1–a2 are overlaid from the magenta solid lines panels a3–a4 for easier comparison between hot and cold patches).

magenta solid lines in panels a3–a4 for easier comparison between hot and cold patches). Figures 2a1–2a4 show that the occurrence of both cold and hot patches is clearly dependent on IMF By. For IMF By < 0 the polar cap patches have a preference for the duskside. For IMF By > 0 the patches have a preference for the dawnside. In Figures 2a1–2a4 the hot patches (magenta lines) seem to be observed at a lower MLAT than the cold patches (black lines). Consequently, the hot patches occur closer to the poleward boundary of the auroral oval.

Table 1 shows the mean MLAT of the cold patches, the hot patches, and the poleward auroral boundary in the dawnside and duskside sector for each of the eight different IMF orientations presented in Figure 1. On the dawnside, the hot patches are on average ~1.7° MLAT equatorward of the cold patches and ~5° MLAT poleward of the auroral oval. On the duskside, the hot patches are on average ~1.8° MLAT equatorward of the cold patches and ~3.5° MLAT poleward of the auroral oval.

Figures 2b1–2b4 show that the cold patches have slightly higher O$^+$ density than the hot patches (Zhang, Xing et al., 2020). Figures 2c1–2c4 show that the hot patches have higher electron temperature than the cold patches (e.g., Ma, Zhang, Xing, Heelis et al., 2018; Zhang et al., 2017). Figures 2d3 and 2d4 indicate that the hot patches are associated with significant fluxes of soft-electron (<1 keV) precipitation around 76–82 MLAT when IMF Bz is positive, which corresponds to high electron temperature in Figures 2c3 and 2c4. Only a weak flux of soft-electron precipitation is seen for the cold patches in Figures 2d1 and 2d2. Figures 2e1–2e4 indicates that the cold patches generally have higher anti-sunward velocities than the hot patches (Zou et al., 2015).

To investigate the influence of local plasma transport and particle precipitation, we studied the relationship between the patch occurrence, $V_{cross-track}$, and the soft-electron energy flux. Figure 3 shows the occurrence of patches versus $V_{cross-track}$ and soft-electron energy flux for cold patches (blue bars), for hot patches (red bars), and for the background (gray bars). The blue and red dotted lines show the relative occurrence rate of the cold and hot patches, respectively. Figures 3a and 3b correspond to southward IMF, and Figures 3c and 3d correspond

Table 1
The Mean MLAT of Cold Patches, Hot Patches, and the Poleward Auroral Boundary in the Dawnside and Duskside Sector for Each of the Eight Different IMF Orientations Presented in Figure 1

MLT \ MLAT / IMF		Bz-	By-/Bz-	By-	By-/Bz+	Bz+	By+/Bz+	By+	By+/Bz-
The mean MLAT of cold patches, hot patches, and the poleward auroral boundary in the dawnside and duskside sector									
Cold patch	6-12	82.85	83.41	82.90	81.58	82.20	82.15	82.67	82.74
	12-18	81.64	82.37	81.70	82.32	82.37	81.22	82.09	82.73
Hot patch	6-12	79.95	80.20	80.15	80.32	80.78	81.98	81.54	81.98
	12-18	79.75	80.31	81.37	80.02	80.65	81.30	79.71	79.11
Poleward Auroral Boundary	6-12	75.55	75.68	75.97	76.24	76.34	76.21	75.93	75.65
	12-18	76.49	76.62	76.87	77.10	77.17	77.04	76.80	76.57

Note. MLAT, magnetic latitude (MLAT).
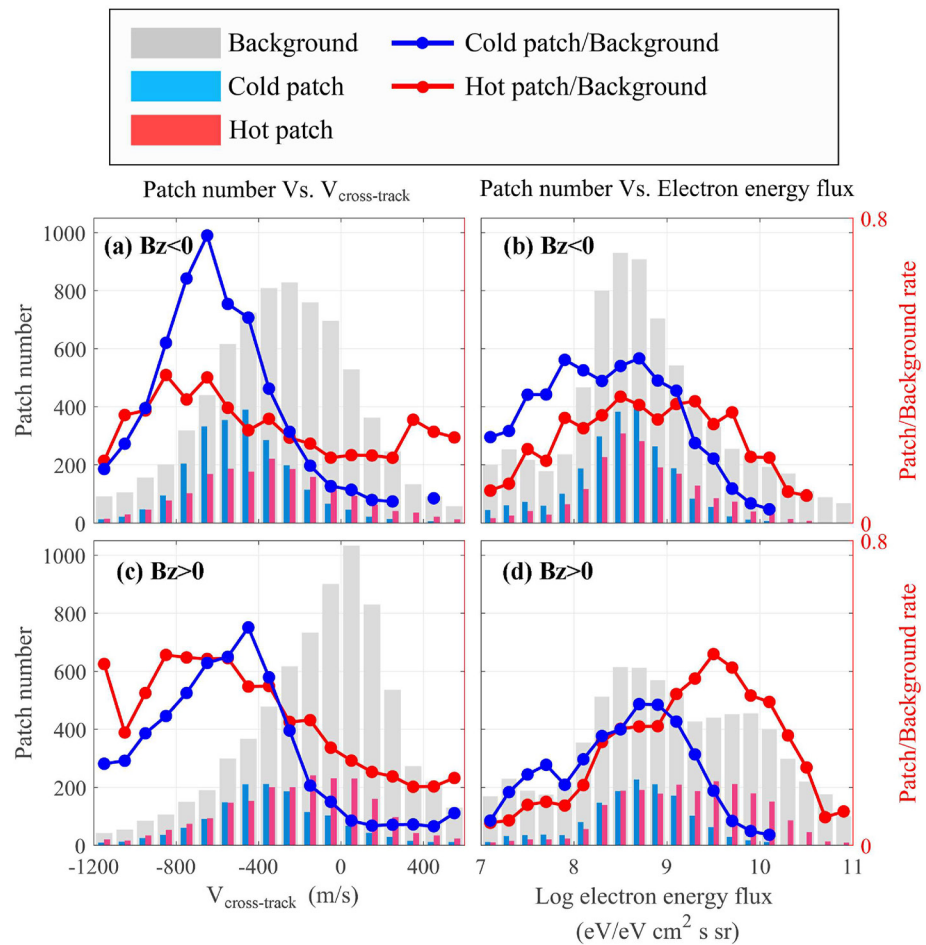
Figure 3. Occurrence of polar cap patches versus (a and c) anti-sunward velocity and (b and d) soft-electron energy flux. Panels a and b correspond to southward interplanetary magnetic field (IMF) (i.e., more negative velocity), and panels c and d correspond to northward IMF. Blue bars indicate cold patches, red bars indicate hot patches, and gray bars show the background. The dotted blue and red lines show the relative occurrence rates of the cold and hot patches, respectively.

to northward IMF. Figure 3a suggests that cold patches' occurrence is higher when the anti-sunward velocity is from ~200 to ~1,000 m/s under southward IMF. Figures 3b and 3d show that hot patches' occurrence is higher when the soft-electron energy flux is larger than 10^9 eV/eV cm^2 s sr both under southward and northward IMF.

4. Discussion

The spatial distributions of cold and hot patches respond well to the IMF convection patterns, and more patches occur in the stronger anti-sunward flow as seen from Figure 1. Many studies have pointed out that patches move along the ionospheric convection streamlines from the dayside to nightside after formation, which is related to magnetic reconnection (Hosokawa et al., 2009; Oksavik et al., 2010; Zhang, Xing et al., 2020). During southward IMF, magnetic reconnection takes place at the low-latitude magnetopause. The newly opened field lines rebound to high latitudes due to the magnetic field tension forces and transport high-density plasma patches poleward along convection streamlines (Zhang, Xing et al., 2020; Zhang, Zhang, Lockwood et al., 2013). Consequently, both cold and hot patches occur most frequently in the stronger anti-sunward flow region of the IMF convection patterns. For positive IMF Bz dominated patches seem to not only be in the regions of anti-sunward flow. This may be due to the convection model limitations. We can see the convection pattern in Figure 1b has weaker electric field and reverse cells, which is similar to Figures 1a and 1c except that Figures 1a and 1c show some of the By dependence seen for small and positive Bz. Moreover, the more patch regions in Figures 1a–1c also show the similar By dependence seen for small and positive Bz. The patch occurrence regions in Figure 1b show enhancements in both the region seen for negative By and in the region seen for positive By. This may result from weaker anti-sunward flow associated with relatively small IMF By, while, the convection pattern in Figure 1b cannot show these regions of enhanced flows, as in Figures 1a and 1c. This is likely because the convection pattern in Figure 1b is built from both ±IMF By (average By ≈ 0).

Figures 2a1–2a4 and Table 1 show that the hot patches occur at lower MLAT than cold patches and closer to the poleward auroral boundary. There are two possible reasons: (a) The hot patches are mainly stimulated by particle precipitation. Transient structures like PMAFs represent enhanced particle precipitation and usually occur near the auroral oval (e.g., Oksavik et al., 2015; Xing et al., 2013). The enhanced particle precipitation usually increases the electron temperature, giving hot patches as have been observed to be induced by PMAFs (e.g., Hosokawa et al., 2016; Lorentzen et al., 2010). Such hot patches, which are associated with particle precipitation close to the auroral oval, may thus lie close to the auroral oval. (b) Some hot patches may also be observed in their initial creation phase with high electron temperature, but as they travel further into the polar cap, due to the lack of a heating source, the electron temperature may fade toward that of the level of cold patches (e.g., Ma, Zhang, Xing, Jayachandran et al., 2018; Zhang et al., 2017).

Figures 2a1–2a4 also indicate a clear prenoon-postnoon asymmetry in the occurrence of both cold and hot patches due to IMF By. When IMF By is negative, the newly opened tubes are pulled into the dusk sector in the NH. For positive IMF By the flux tubes are pulled into the dawn sector (e.g., Jin et al., 2019; Southwood, 1987; Xing et al., 2013). Moreover, some plasma features like the soft-electron (<1 keV) energy flux and $V_{\text{cross-track}}$ will also respond to the sign of IMF By.

Figures 2b1–2b4 show that the cold patches have higher O$^+$ density than the hot patches. This may indicate the different formation mechanisms of the two type patches: the cold patches are generated from midlatitude ionospheric plasma produced by solar extreme ultraviolet radiation (EUV); while the hot patches are associated with local particle precipitation. The EUV plasma is typically denser than plasma generated through precipitation (Zhang, Xing et al., 2020).

Figures 2d3 and 2d4 show enhanced soft-electron precipitation around 76–82 MLAT for hot patches when IMF Bz is positive, which corresponds to high electron temperature in Figures 2c3 and 2c4. The enhanced soft-electron energy flux is a heat source for the topside electrons that will increase the electron temperature (Seo et al., 1997). The enhanced electron precipitation for IMF Bz positive is likely associated with lobe reconnection resulting in more particle precipitation in the polar cap (Lockwood & Moen, 1999; Xing et al., 2018; Zhang, Zhang et al., 2020).

Figure 3 shows that cold patch occurrence is higher when the anti-sunward velocity is between 200 and 1,000 m/s under southward IMF, or the soft-electron energy flux is lower than 10^9 eV/eV cm^2 s sr both under southward

and northward IMF. Higher anti-sunward flow velocity facilitates easy transport of cold patches from dayside sunlit areas. When the anti-sunward velocity exceeds ∼1,000 m/s, it may also increase the electron temperature (Kofman & Wickwar, 1984). Under northward IMF, the speed of background anti-sunward flow is low which results in the highest occurrence of cold patches appearing in the flow regions of $-300 \sim -600$ m/s. It seems that the enhanced anti-sunward flow also contributes to the hot patches. Due to the existence of the reverse cells under northward IMF, the polar cap region appears more sunward flow, and the ionospheric convection patterns are more complicated. This should be investigated in more depth in future studies. The hot patches are stimulated by particle precipitation, so larger soft-electron energy flux is favorable for higher occurrence of hot patches.

5. Conclusions

We analyzed the winter patches of DMSP F16 database of Zhang et al. (2021) to investigate the relationship between polar cap patch occurrence, IMF orientation, ionospheric convection, and particle precipitation. The spatial distributions of cold and hot patches respond well to statistical IMF convection patterns. The hot patches seem to occur closer to the auroral oval and at lower magnetic latitudes than the cold patches. There is a clear correspondence between the enhanced soft-electron precipitation and high electron temperature in the hot patches. The high anti-sunward flow ($E \times B$ drift) mainly contributes to increased occurrence of cold patches under southward IMF, while the soft-electron precipitation mainly contributes to the occurrence of hot patches both under southward and northward IMF.

Data Availability Statement

The SuperDARN data are obtained from http://superdarn.thayer.dartmouth.edu/models/PSR10.html. The NOAA FTP and JHU/APL (https://satdat.ngdc.noaa.gov/dmsp/data/) and CEDAR Madrigal (http://cedar.openmadrigal.org/list/) provide available DMSP data (by registering your personal information, and searching for "Satellite Instruments" in the box of "Choose instrument category(s)" and "Defense Meteorological Satellite Program [1982–2021]" in the box of "Choose instrument(s)," then clicking the "list experiments"). The NASA OMNI (http://omniweb.gsfc.nasa.gov) provides available IMF data. The auroral oval model are obtained from http://www.geophy.cn/article/doi/10.6038/cjg20160203. The event list of cold and hot patches is available in https://doi.org/10.5281/zenodo.6511063.

References

Carlson, H. C. (2012). Sharpening our thinking about polar cap ionospheric patch morphology, research, and mitigation techniques. *Radio Science*, *47*, RS0L21. https://doi.org/10.1029/2011RS004946

Carlson, H. C., Oksavik, K., Moen, J., & Pedersen, T. (2004). Ionospheric patch formation: Direct measurements of the origin of a polar cap patch. *Geophysical Research Letters*, *31*(8), L08806. https://doi.org/10.1029/2003GL018166

Coley, W. R., & Heelis, R. A. (1995). Adaptive identification and characterization of polar ionization patches. *Journal of Geophysical Research*, *100*(A12), 23819–23827. https://doi.org/10.1029/95JA02700

Crowley, G. (1996). A critical review of ionospheric patches and blobs. In *Review of radio science 1993–1996* (pp. 619–648). Oxford University Press.

Dungey, W. J. (1961). The steady state of the Chapman-Ferraro problem in two dimensions. *Journal of Geophysical Research*, *66*(4), 1043–1047.

Goodwin, L. V., Iserhienrhien, B., Miles, D. M., Patra, S., van der Meeren, C., Buchert, S. C., et al. (2015). Swarm in situ observations of F region polar cap patches created by cusp precipitation. *Geophysical Research Letters*, *42*, 996–1003. https://doi.org/10.1002/2014GL062610

Greenspan, M. E., Anderson, P. B., & Pelagatti, J. M. (1986). *Characteristics of the thermal plasma monitor (SSIES) for the Defense meteorological satellite Program (DMSP) spacecraft S8 through F10*. Tech. Rep. AFGL- TR-86- 0227. Hanscom AFB.

Hardy, D. A., Schmitt, L. K., Gussenhoven, M. S., Marshall, F. J., & Yeh, H. C. (1984). *Precipitating electron and ion detectors (SSJ/4) for the block 5D/flights 6-10 DMSP (Defense Meteorological Satellite Program) satellites: Calibration and data presentation*. Rep. AFGL-TR-84-0317. Air Force Geophys. Lab., Hanscom Air Force Base, Mass.

Hosokawa, K., Kashimoto, T., Suzuki, S., Shiokawa, K., Otsuka, Y., & Ogawa, T. (2009). Motion of polar cap patches: A statistical study with all-sky airgolw imager at Resolute Bay, Canada. *Journal of Geophysical Research*, *114*, A04318. https://doi.org/10.1029/2008JA014020

Hosokawa, K., Taguchi, S., & Ogawa, Y. (2016). Periodic creation of polar cap patches from auroral transients in the cusp. *Journal of Geophysical Research: Space Physics*, *121*, 5639–5652. https://doi.org/10.1002/2015JA022221

Hu, Z.-J., Yang, Q.-J., Liang, J.-M., Hu, H.-Q., Zhang, B.-C., & Yang, H.-G. (2017). Variation and modeling of ultraviolet auroral oval boundaries associated with interplanetary and geomagnetic parameters. *Space Weather*, *15*, 606–622. https://doi.org/10.1002/2016SW001530

Jin, Y.-Y., Xing, Z.-Y., Zhang, Q.-H., Wang, Y., & Ma, Y.-Z. (2019). Polar cap patches observed by the EISCAT Svalbard Radar: A statistical study of its dependence on the solar wind and IMF conditions. *Journal of Atmospheric and Solar-Terrestrial Physics*, *192*, 104768. https://doi.org/10.1016/j.jastp.2018.01.011

Kofman, W., & Wickwar, V. B. (1984). Very high electron temperatures in the daytime F region at Sondrestrom. *Geophysical Research Letters*, *11*(9), 919–922. https://doi.org/10.1029/GL011i009p00919

Lockwood, M., & Carlson, H. C. (1992). Production of polar cap electron density patches by transient magnetopause reconnection. *Geophysical Research Letters*, *19*(17), 1731–1734. https://doi.org/10.1029/92GL01993

Lockwood, M., & Moen, J. (1999). Reconfiguration and closure of lobe flux by reconnection during northward IMF: Possible evidence for signatures in cusp/cleft auroral emissions. *Annales Geophysicae*, *17*(8), 996–1011. https://doi.org/10.1007/s00585-999-0996-2

Lorentzen, D. A., Moen, J., Oksavik, K., Sigernes, F., Saito, Y., & Johnsen, M. G. (2010). In situ measurement of a newly created polar cap patch. *Journal of Geophysical Research*, *115*, A12323. https://doi.org/10.1029/2010ja015710

Ma, Y.-Z., Zhang, Q.-H., Xing, Z.-Y., Heelis, R. A., Oksavik, K., & Wang, Y. (2018). The ion/electron temperature characteristics of polar cap classical and hot patches and their influence on ion upflow. *Geophysical Research Letters*, *45*(6), 8072–8080. https://doi.org/10.1029/2018GL079099

Ma, Y.-Z., Zhang, Q.-H., Xing, Z.-Y., Jayachandran, P. T., Moen, J., Heelis, R. A., & Wang, Y. (2018). Combined contribution of solar illumination, solar activity, and convection to ion upflow above the polar cap. *Journal of Geophysical Research: Space Physics*, *123*, 4317–4328. https://doi.org/10.1029/2017JA024974

Mandea, M., & Macmillan, S. (2000). International geomagnetic reference field—The eighth generation. *Earth Planets and Space*, *52*, 1119–1124. https://doi.org/10.1186/BF03352342

McEwen, D. J., & Harris, D. P. (1996). Occurrence patterns of F layer patches over the north magnetic pole. *Radio Science*, *31*(3), 619–628. https://doi.org/10.1029/96rs00312

Nishimura, Y., Lyons, L. R., Zou, Y., Oksavik, K., Moen, J. I., Clausen, L. B., et al. (2014). Day-night coupling by a localized flow channel visualized by polar cap patch propagation. *Geophysical Research Letters*, *41*, 3701–3709. https://doi.org/10.1002/2014GL060301

Oksavik, K., Barth, V. L., Moen, J., & Leste, M. (2010). On the entry and transit of high-density plasma across the polar cap. *Journal of Geophysical Research*, *115*, A12308. https://doi.org/10.1029/2010JA015817

Oksavik, K., van der Meeren, C., Lorentzen, D. A., Baddeley, L. J., & Moen, J. (2015). Scintillation and loss of signal lock from poleward moving auroral forms in the cusp ionosphere. *Journal of Geophysical Research: Space Physics*, *120*, 9161–9175. https://doi.org/10.1002/2015JA021528

Pettigrew, E. D., Shepherd, S. G., & Ruohoniemi, J. M. (2010). Climatological patterns of high-latitude convection in the Northern and Southern hemispheres: Dipole tilt dependencies and interhemispheric comparisons. *Journal of Geophysical Research*, *115*, A07305. https://doi.org/10.1029/2009JA014956

Seo, Y., Horwitz, J. L., & Caton, R. (1997). Statistical relationships between high-latitude ionospheric F region/topside upflows and their drivers: DE 2 observations. *Journal of Geophysical Research*, *102*(A4), 7493–7500. https://doi.org/10.1029/2019JA027449

Southwood, D. J. (1987). The ionospheric signature of flux transfer events. *Journal of Geophysical Research*, *92*(A4), 3207–3213. https://doi.org/10.1029/JA092iA04p03207

Spicher, A., Clausen, L. B. N., Miloch, W. J., Lofstad, V., Jin, Y., & Moen, J. I. (2017). Interhemispheric study of polar cap patch occurrence based on Swarm in situ data. *Journal of Geophysical Research: Space Physics*, *122*, 3837–3851. https://doi.org/10.1002/2016JA023750

Weber, E. J., Buchau, J. J., Moore, J. G., Sharber, J. R., Livingston, R. C., Winningham, J. D., & Reinish, B. W. (1984). F layer ionization patches in the polar cap. *Journal of Geophysical Research*, *89*(A3), 1683–1694. https://doi.org/10.1029/JA089iA03p01683

Xing, Z., Zhang, Q., Han, D., Zhang, Y., Sato, N., Zhang, S., et al. (2018). Conjugate observations of the evolution of polar cap arcs in both hemispheres. *Journal of Geophysical Research: Space Physics*, *123*, 1794–1805. https://doi.org/10.1002/2017JA024272

Xing, Z.-Y., Yang, H.-G., Han, D.-S., Wu, Z.-S., Liu, J.-M., Hu, Z.-J., et al. (2013). Dayside poleward moving auroral forms and ionospheric convection under stable interplanetary magnetic field (IMF) conditions. *Science China Technological Sciences*, *56*, 910–916. https://doi.org/10.1007/s11431-013-5164-y

Yang, Q.-J., Hu, Z.-J., Han, D.-S., Hu, H., & Xiao, M. (2016). Modeling and prediction of ultraviolet auroral oval boundaries base on IMF/solar wind and geomagnetic parameters. *Chinese Journal of Geophysics*, *59*(2), 426–439. (In Chinese). https://doi.org/10.6038/cjg20160203

Zhang, D., Zhang, Q.-H., Ma, Y.-Z., Oksavik, K., Lyons, L. R., Zhang, Y.-L., et al. (2021). Solar and geomagnetic activity impact on occurrence and spatial size of cold and hot polar cap patches. *Geophysical Research Letters*, *48*, e2021GL094526. https://doi.org/10.1029/2021GL094526

Zhang, Q.-H., Lockwood, M., Foster, J. C., Zhang, S.-R., Zhang, B.-C., McCrea, I. W., et al. (2015). Direct observations of the full Dungey convection cycle in the polar ionosphere for southward interplanetary magnetic field condition. *Journal of Geophysical Research: Space Physics*, *120*, 4519–4530. https://doi.org/10.1002/2015JA021172

Zhang, Q.-H., Ma, Y.-Z., Jayachandran, P. T., Moen, J., Lockwood, M., Zhang, Y.-L., et al. (2017). Polar cap hot patches: Enhanced density structures different from the classical patches in the ionosphere. *Geophysical Research Letters*, *44*, 8159–8167. https://doi.org/10.1002/2017GL073439

Zhang, Q.-H., Moen, J. I., Lockwood, M., McCrea, I., Zhang, B.-C., McWilliams, K. A., et al. (2016). Polar cap patch transportation beyond the classic scenario. *Journal of Geophysical Research: Space Physics*, *121*, 9063–9074. https://doi.org/10.1002/2016JA022443

Zhang, Q.-H., Xing, Z.-Y., Wang, Y., & Ma, Y.-Z. (2020). Formation and evolution of polar cap ionospheric patches and their associated upflows and scintillations: A review. In Q. G. Zong, P. Escoubet, D. Sibeck, G. Le, & H. Zhang (Eds.), *Dayside magnetosphere interaction* (pp. 286–302). John Wiley & Sons, Inc. https://doi.org/10.1002/9781119509592.ch16

Zhang, Q.-H., Zhang, B.-C., Hu, H.-Q., Moen, J., Lockwood, M., Yang, H. G., et al. (2013). Polar cap patch segmentation of the tongue of ionization in the morning convection cell. *Geophysical Research Letters*, *40*, 2918–2922. https://doi.org/10.1002/grl.50616

Zhang, Q.-H., Zhang, B.-C., Liu, R.-Y., Dunlop, M. W., Lockwood, M., Moen, J., et al. (2010). On the importance of interplanetary magnetic field vertical bar B-y vertical bar on polar cap patch formation. *Journal of Geophysical Research*, *116*, A05308. https://doi.org/10.1029/2010JA016287

Zhang, Q.-H., Zhang, B.-C., Lockwood, M., Hu, H.-Q., Moen, J. I., Ruohoniemi, J. M., et al. (2013). Direct observations of the evolution of polar cap ionization patches. *Science*, *339*(6127), 1597–1600. https://doi.org/10.1126/science.1231487

Zhang, Q.-H., Zhang, Y.-L., Wang, C., Lockwood, M., Yang, H.-G., Tang, B.-B., et al. (2020). Multiple transpolar auroral arcs reveal insight about coupling processes in the Earth's magnetotail. *Proceedings of the National Academy of Sciences of the United States of America*, *117*(28), 16193–16198. https://doi.org/10.1073/pnas.2000614117

Zou, Y., Nishimura, Y., Lyons, L. R., Shiokawa, K., Donovan, E. F., Ruohoniemi, J. M., et al. (2015). Localized polar cap flow enhancement tracing using airglow patches: Statistical properties, IMF dependence, and contribution to polar cap convection. *Journal of Geophysical Research: Space Physics*, *120*, 4064–4078. https://doi.org/10.1002/2014JA020946